

## Optical Spectroscopic Observations of Cyg X-1=HDE 226868

Jingzhi Yan<sup>1</sup>, Qingzhong Liu<sup>1</sup> and Petr Hadrava<sup>2</sup>

### ABSTRACT

We present the results of the spectroscopic observations of HDE 226868, the optical counterpart to the black hole X-ray binary Cyg X-1, from 2001 to 2006. We analyze the variabilities of the two components in the complex H $\alpha$  line: one P-Cygni shaped component which follows the motion of the supergiant and another emission component moving with an antiphase orbital motion relative to the supergiant, which is attributed to a focused-stellar wind. The results of KOREL disentangling of our spectra indicate that the focused stellar wind is responsible for the major part of the variability of the H $\alpha$  emission line. The emission of the supergiant component had a small difference between the low/hard and high/soft states, while the focused wind component became strong in the low/hard state and weak in the high/soft state. The wind is nearly undisturbed by the X-ray photoionization during the low/hard state. However, during the high/soft state, the X-rays from the compact object could decelerate the line-driven wind and result in a high mass accretion rate, due to the effect of the X-ray photoionization. The X-ray illuminating could also change the temperature profile of the stellar wind and increase its temperature, and thus decrease the H $\alpha$  emissivity of the wind, which could explain the H $\alpha$  variabilities of Cyg X-1 during different X-ray states.

*Subject headings:* Stars: Binaries: Spectroscopic, Stars: Early-Type, stars: individual (HDE 226868, Cygnus X-1), Stars: Winds, Outflows, X-Rays: Binaries

### 1. INTRODUCTION

Cygnus X-1 was first discovered during a rocket flight observation in 1964 (Bowyer et al. 1965) and its optical counterpart was identified with the supergiant star HDE 226868 (Bolton 1972; Webster & Murdin 1972). A 5.6d orbital period was found in the optical spectroscopic observations (Gies & Bolton 1982) and the dynamical determination of the binary components provided evidence for the existence of a black hole in Cyg X-1. As the black hole X-ray binary, which was first found

---

<sup>1</sup>Purple Mountain Observatory, Chinese Academy of Sciences, Nanjing , China; jzyan@pmo.ac.cn, qzliu@pmo.ac.cn

<sup>2</sup>Astronomical Institute, Academy of Sciences, Boční II 1401, CZ-14131 Prague, Czech Republic; had@sunstel.asu.cas.cz

in our Galaxy, Cyg X-1 has been extensively studied from radio to  $\gamma$ -rays during recent decades. Even though the mass function is precisely known (see Gies et al. (2003)), the masses of the donor star and the black hole are not so well constrained due to the poorly known inclination and the evolutionary status of the supergiant. Using the inclination of  $i = 35^\circ$ , Herrero et al. (1995) estimated the masses of the supergiant and the black hole at  $17.8 M_\odot$  and  $10.1 M_\odot$ , respectively.

HDE 226868 was classified as an O9.7 Iab supergiant star (Walborn 1973), which shows H $\alpha$  and He II  $\lambda 4686$  in emission. Although the supergiant nearly fills the Roche lobe, the accretion is mainly via the strong stellar wind from the donor star (Gies & Bolton 1986a; Gies et al. 2003). The variabilities of the optical lines (Gies & Bolton 1986b; Ninkov et al. 1987) on the spectrum of HDE 226868 indicate that the distribution of the stellar wind deviates from a spherical geometry and that an enhanced wind flow exists (“focused stellar wind,” suggested by Friend & Castor (1982)) in the direction of the compact object. The focused stellar wind is also revealed by the High-Energy Transmission Grating Spectrometer aboard the Chandra X-Ray Observatory (Miller et al. 2005).

The most recent ephemeris of the 5.6d orbital period has been given by LaSala et al. (1998), Brocksopp et al. (1999b), and Gies et al. (2003) according to their optical spectroscopic observations. In addition, the 5.6d orbital period is also found in the *UBVJHK* photometry, X-ray and radio data of Cyg X-1 (Brocksopp et al. 1999a). Cyg X-1 also shows the superorbital modulation, on a time-scale much longer than the orbital period. A 294d period was first reported by Priedhorsky et al. (1983) in X-rays and then by Kemp et al. (1983) in the optical. Another  $\sim 150$ d period was found by different authors (Brocksopp et al. 1999a; Lachowicz et al. 2006) in X-ray and radio data. This  $\sim 150$  d period may be caused by the precession of the accretion disk around the compact object (Wijers & Pringle 1999).

A relativistic radio jet with a velocity larger than  $\sim 0.6c$  was detected by Stirling et al. (2001) in their radio observations of Cyg X-1, and therefore Cyg X-1 joins the group of the Galactic microquasar. Microquasar is an X-ray binary with a pair of relativistic radio jets, which is similar to the radio jets found in the active galactic nuclei (see Mirabel & Rodríguez (1999) for a review). The jet remnant of Cyg X-1 is resolved in radio (Gallo et al. 2005) and optical (Russell et al. 2007) observations.

Many observational characteristics of the canonical stellar black hole candidate Cyg X-1 are considered evidence that a black hole exists, similar to other X-ray binary systems. These observational features include the ultra-soft spectra, the high-energy power-law tail above 20 keV, the spectral/temporal transition from the high/soft state to the low/hard state and the X-ray millisecond variability (see Tanaka & Lewin (1995); McClintock & Remillard (2006); Remillard & McClintock (2006)). Most of the time Cyg X-1 is in a low/hard state and in some years it can transit from the low/hard state to the high/soft state, which can continue from several weeks to several months (Zhang et al. 1997; Brocksopp et al. 1999a). Occasionally, Cyg X-1 enters an intermediate state when it fails to make a transition from the low/hard state to the high/soft state (Belloni et al. 1996; Malzac et al. 2006). The radio and X-ray emission has an anticorrelation and when the bi-

nary enters the high/soft state, the radio emission will be decreased (Pooley 2001). Most researchers believe the transition state is caused by the physical changes of the gas around the black hole (see Remillard & McClintock (2006) and references therein). The physical changes in the accretion disk are initially related to the mass loss from the supergiant companion. However, the X-ray radiation of the disk influences the ionization and temperature of the wind and thus also its radiation and dynamics.

Using the method of tomographic separation<sup>1</sup> (Bagnuolo & Gies 1991), Sowers et al. (1998) showed that the H $\alpha$  profiles of Cyg X-1 observed in seasons 1985 and 1986 can be well fitted as a superposition of a P-Cyg profile corresponding to the (approximately spherical) stellar wind of the supergiant and a wide emission peak radiated by the focused stellar wind, which moves in a slightly shifted anti-phase with respect to the orbital Doppler shift of the former component. Using the method of Fourier disentangling (Hadrava 1995, 1997, 2004) we have proved the same behavior in the spectra obtained at Ondřejov Observatory in summer 2003 shortly before, during and shortly after one high/soft-state episode of Cyg X-1 (Hadrava 2007).

In this article, we present our optical spectroscopic observations of Cyg X-1 from 2001 to 2006. The preliminary results have been introduced in a previous article (Yan, Liu & Hang 2005). Here we will make a further analysis of the H $\alpha$  line profiles. Our present data are confined to about one week in each season, meaning they are concentrated into only slightly more than one orbital period. This enables us to compare the solutions of disentangling in different X-ray states, minimizing the possible influence of long-term variations in the structure of the focused stellar wind.

In the following section, the properties of our data are described. The method and results of the disentangling are given in Section 3. Next, the correspondence of our observational results with the standard model of this classical X-ray binary is studied in Section 4. Finally, the conclusions are summarized in Section 5.

## 2. OBSERVATIONS

We obtained the spectra of HDE 226868 with the 2.16m telescope at Xinglong Station of National Astronomical Observatories, China (NAOC), from 2001 to 2006. The optical spectroscopy with an intermediate resolution of  $1.22 \text{ \AA pixel}^{-1}$  was made with a CCD grating spectrograph at the Cassegrain focus of the telescope. We took the red spectra covering from 5500 to 6700  $\text{\AA}$  and blue spectra covering from 4300 to 5500  $\text{\AA}$  at different times. Sometimes low-resolution spectra (covering from 4300 to 6700  $\text{\AA}$ ) were also obtained. The journal of our observations is summarized in Table 1, including observational date, UT Middle, exposure time, Julian date, wavelength range,

---

<sup>1</sup> This method of decomposition of observed spectra into unknown spectra of two components should be distinguished from the methods of Doppler tomography in which the phase-locked line-profile variations are fitted by projections of smooth distribution of delta-function profiles in velocity space corotating with the orbital motion.

and spectral resolution. Orbital phase ( $\phi$ ) is also given in Table 1 and the ephemeris of the inferior conjunction of the companion star is adopted from Gies et al. (2003),

$$2,451,730.449 + 5.599829E .$$

All spectroscopic data were reduced with the IRAF<sup>2</sup> package. They were bias-subtracted and flat-field corrected, and had cosmic rays removed. Helium-argon spectra were taken in order to obtain the pixel-wavelength relations. To improve this relation, we also used the diffuse interstellar bands (DIBs) 6614 and 6379 Å observed in the spectra.

The higher resolution red spectra obtained from 2001 to 2006 are shown in Figure 1. The corresponding observational dates and orbital phases calculated according to the above given ephemeris are written on the left and right sides of each spectrum, respectively. The spike on the left part of the spectrum on 2002 October 26 may be caused by a cosmic hot point and the dips on the spectra of 2004 September 21 are caused by bad pixels on the CCD. Most of the H $\alpha$  lines show a double-peaked profile with a central absorption. Single-peaked H $\alpha$  lines are observed in our spectra of 2003 October 14 ( $\phi=0.67$ ), 2005 October 24 ( $\phi=0.004$ ) and 2006 September 29 ( $\phi=0.72$ ). Obvious P-Cygni H $\alpha$  lines are observed in our spectra in some phases only in 2004 (Figure 1(c)).

For a comparison, we have also used the spectra obtained with the 700mm camera of the Coudé spectrograph at the 2.05m telescope of the Ondřejov observatory (the Astronomical Institute of the Czech Academy of Sciences). These spectra covering the region 6260–6760 Å with a resolution of approximately  $0.25 \text{ \AA pixel}^{-1}$  are included in a study by Gies et al. (2008), to which we refer for details.

### 3. ANALYSIS AND RESULTS

#### 3.1. The Equivalent Width Evolution of H $\alpha$ and the X-ray Activity

The equivalent width (EW) of the complex H $\alpha$  line (emission and absorption) has been measured selecting a continuum point on each side of the line and integrating the flux relative to the straight line between the two points using the procedures available in IRAF. The measurements were repeated five times for each spectrum and the error estimated from the distribution of values obtained. The typical error for H $\alpha$  measurements is within 10%. This error arises due to the subjective selection of the continuum. The results of H $\alpha$  EWs are listed in Table 1.

The top panel of Figure 2 shows the variability of the H $\alpha$  EW from 2001 to 2006 as a function of time. In addition to the data obtained in our observational program, the combined data sets of Gies et al. (2003) and Tarasov et al. (2003) are also included in the figure. For a comparison, the

---

<sup>2</sup>IRAF is distributed by NOAO, which is operated by the Association of Universities for Research in Astronomy, Inc., under cooperation with the National Science Foundation.

middle panel of Figure 2 gives the RXTE/ASM one-day averaged counter rate in the 1.5-12 keV band and the hardness ratio (HR1) of the soft X-ray radiation, (3-5 keV)/(1.5-3 keV) is plotted in the bottom panel. The arrows in this panel correspond to the starting date of each observational run.

Figure 2 shows that our 2001 and 2004 observational runs were done in a high/soft state while 2003, 2005, and 2006 observational runs in a low/hard state. The observations in 2002 were during a transitional state from high/soft to low/hard. The EW of H $\alpha$  is relatively low in the high/soft state and strong in the low/hard state. This phenomenon has been discussed in detail by Gies et al. (2003) and Tarasov et al. (2003). While the H $\alpha$  in our spectra of 2001 nearly lost its emission signature, the emission level of H $\alpha$  in the 2006 observations is the strongest among our six observational runs. Because the season 2001 is poorly covered by observations, we chose the observational runs 2004 and 2006 to represent the high/soft and low/hard states, respectively, in our study of line-profile variability.

### 3.2. The Profile Variability of H $\alpha$ Emission Line

The top panel of Figure 3 shows the H $\alpha$  profiles during our 2006 observational run. The exposures are depicted in ascending order according to the orbital phase. The observational date and orbital phase are marked on the left and right sides of each spectrum, respectively. We have recalibrated the wavelength scale of each spectrum according to the position of the DIB 6614 Å. It can be seen from this figure that, for most of the time, the H $\alpha$  of Cyg X-1 has a double-peaked profile, one peak formed in the supergiant and the other in the focused stellar wind between the system components (Sowers et al. 1998; Gies et al. 2003). As in many other supergiants, its intrinsic H $\alpha$  emission is due to the powerful stellar wind (Puls et al. 1996) and it forms the red-shifted emission wing of the P-Cygni line profile that follows the orbital motion of the star. In some phases (e.g., 0.720, which is close to one extreme of the radial velocities), this emission merges with the emission of the focused wind moving almost in an anti-phase and they form a single bright peak. In some other phases, the emission of the focused wind can fill the absorption part of the P-Cygni component formed in the supergiant. Thus we can detect a characteristic P-Cygni H $\alpha$  line in the spectrum of Cyg X-1 only in some phases of the high/soft state, when the focused-wind emission is weak. The bottom panel of Figure 3 shows a gray-scale map of the H $\alpha$  profiles in 2006.

Following Sowers et al. (1998), Gies et al. (2003) used the tomographic separation algorithm to decompose the H $\alpha$  line profile into the two components for chosen combinations of the radial velocity semiamplitude  $K_{em}$  and phase shift  $\phi$  of the focused wind (orbital parameters of the supergiant being fixed from nonemission lines). Minimizing the residuals in the two-parameter space, they found that the focused wind component has a maximum radial velocity  $K_{em} = 218 \pm 30 \text{ km s}^{-1}$  near the orbital phase  $\phi_0 = 0.79 \pm 0.04$ . The radial velocity curves of the two components are plotted in Figure 4. The positions of the focused-wind component of the H $\alpha$  line based on this solution are also marked by ticks in Figure 1.

### 3.3. Disentangling the $H\alpha$ Line Profile

The methods of disentangling fit the observed spectra as a superposition of several components with simultaneously optimized orbital parameters (and/or some other free parameters). Usually, the emission-line objects are variable on a time scale shorter than the orbital period. This creates problems for disentangling, tomographic separation, Doppler imaging or any other similar method that requires observations spanning a time interval at least of this order (unless the variability is properly involved in the model of component spectra). However, there is always a chance that such methods can reveal a mean behavior of the object treating the rapid variability as a noise.

The results by Sowers et al. (1998) and Gies et al. (2003) indicate that this assumption can work well in the case of Cyg X-1. To decompose the spectra of the supergiant and the focused stellar wind, we thus use the KOREL code (Hadrava 2004) for Fourier disentangling (Hadrava 1995), which enables us to take into account and to resolve instantaneous changes in strength of lines of each component (Hadrava 1997). In the preliminary results for the Ondřejov data (Hadrava 2007) the He I line at  $6678 \text{ \AA}$  has been disentangled into a weak telluric contribution and a pure absorption line of the supergiant, which confirms within the observational errors the orbital parameters, found by classical measurements (e.g.,  $K_1 = 71.9 \text{ km s}^{-1}$  compared to  $75.6 \pm .7$  by Gies et al. (2003), or  $73.0 \pm .7$  by Gies et al. (2008)). The  $H\alpha$  line has been disentangled into three components corresponding to the supergiant, the focused wind, and the telluric water vapor lines, which are relatively strong in some Ondřejov spectra. Because, unlike the orbital velocities of the supergiant and the black hole, the mean velocity of the focused stellar wind is not perpendicular to the line joining the components of the binary, the option of KOREL to disentangle up to five components in a hierarchical structure has been used to identify the focused wind with a component of a second close pair corotating with the supergiant-black hole pair with identical period but with a shifted phase. The results showed the P-Cyg profile moving with the supergiant and a broad emission peak of the focused wind. The orbital parameters of the P-Cyg profile converged in the disentangling to values consistent with the He-line solution (e.g.,  $K_1 = 71.3 \text{ km s}^{-1}$ ). The variations of its strength were relatively small (of the order of 0.1); moreover the EW of this component is also small, because the red emission wing nearly compensates the blue absorption wing. For the broad emission component we found a semiamplitude of  $K_{em} = 60.8 \text{ km s}^{-1}$ , which agrees better with the value  $68 \text{ km s}^{-1}$  by Sowers et al. (1998) rather than the value obtained by Gies et al. (2003); compare their figures 5 and 6, respectively. The broad minima of the spectra residuals in the parameter space are due to the large width and the variability of the focused-wind emission component, and the position of the deepest point may be influenced by long-term changes in the circumstellar matter as well as by the random sampling by the observations. The line-strength factor derived by disentangling of the Ondřejov spectra for the focused wind is significantly higher for this component (reaching a value around +1 at the initial and final low/hard  $H\alpha$  emitting states). Because the absolute value of EW of the focused wind (which is negative) is higher, the variability of this component is responsible for the major part of the enhancement of the  $H\alpha$  emission in the low/hard state. In the disentangling of the Ondřejov data, a small part of the  $H\alpha$  emission appeared in the telluric

spectrum, which was left arbitrary to test the behavior of the solution. Because the annual changes of the heliocentric radial velocity corrections are appreciably smaller compared with the amplitudes of both the supergiant and the focused-wind disentangled components, this part of the emission belongs to circumstellar matter which is in the mean at rest with respect to the center of mass of the binary system.

In disentangling the NAOC spectra we struggled with two instrumental obstacles. One was the smaller spectral resolution and the other was the unreliability of the dispersion curve, probably caused by insufficient stiffness of the Cassegrain spectrograph. Due to the former, no telluric lines can be seen in these spectra. Fortunately, it seems that they are not as strong as they are in some Ondřejov spectra, in which they can be distinguished even after a smoothing. Consequently, they do not need to be disentangled to clean the stellar spectra, but at the same time they cannot be used to check or improve the wavelength scale, as described by Hadrava (2006). We thus tried to use the above-mentioned DIBs 6614 and 6379 Å for this purpose. We measured their positions in the Ondřejov spectra first to find their mean central wavelengths in Cyg X-1 and then in the NAOC spectra to get the same values by a linear transformation of the wavelength scale in each of these spectra. For the measurement we used a single-component disentangling by KOREL in the option of free radial velocities in each exposure (e.g., Hadrava (2004)). This procedure improved the wavelength scale to some extent, yet a solution of the He I line 6678 Å made in order to check the reliability of the improved wavelength scale revealed errors in some exposures up to about 60 km s<sup>-1</sup> and similarly the disentangling of H $\alpha$  did not provide satisfactory results. The insufficient precision of the results may be caused by the weakness of the DIB 6379 Å, which was still measurable in the Ondřejov data, but too shallow and wide in the lower-resolution data from the NAOC.

We thus chose an alternative way to disentangle the H $\alpha$  profiles in spite of unreliable wavelength scale. First we disentangled both seasons 2004 and 2006 together with the Ondřejov data for the three components (the supergiant, the focused wind and the telluric lines) in the option of free velocities. The velocities and line strengths were kept fixed for the Ondřejov exposures from their previous standard solution. This solution was thus used as a template to which radial velocities and line strengths of each NAOC exposure were adjusted. The line strengths were also converged by the simplex method (instead of direct least squares which would also change the Ondřejov values) for the first two components in these exposures and prescribed to a large negative value for the telluric component to diminish it in the NAOC exposures. (The difference in spectral resolution of these two data sets proved to be unessential in these wide profiles.) The results of this solution were used as the initial approximation for two component solutions (without the telluric lines) of free radial velocities and line strengths (now by the direct calculation) independently for both seasons 2004 and 2006 without the other data. These solutions thus cannot yield correct radial velocity curves for each component and proper wavelengths of the disentangled spectra, but they give correct differences between the radial velocities of the two components, their line profiles, and the line strengths.

The disentangled H $\alpha$  profiles and the fit of the input spectra for our 2004 and 2006 observations

are plotted by the standard graphical KOREL output in Figure 5 at the left and right panels, respectively. These spectra span from 6540 Å to about 6596 Å; however, the shift of each profile up to several Å is uncertain due to the above-explained problems. It can be seen (at the upper 7 and 11 curves, respectively.) that the agreement of the fit with the observation is quite good (some differences appear for the fifth and sixth exposures from the top in the right panel only, i.e. for 2006 September 28).

The bottom two curves show the disentangled P-Cyg profile of the supergiant (the higher of these two curves) and the mean disentangled emission profile of the focused stellar wind (the very bottom curve) in each season. The tops of the emission wings of the P-Cyg profiles are 1.06 and 1.09 of the level of continuum in 2004 and 2006, resp. This indicates a 50% increase above the continuum in the low/hard state in 2006; however, this result deserves a confirmation by more extensive observations, because the small change representing 3% of the continuum may be influenced only by uncertainties of the continuum intensity (e.g., due to differences in phase sampling). In any case, this change in the P-Cyg component is negligible in comparison with the overall enhancement of H $\alpha$  emission in the low/hard state. The absorption wing is shallower in 2004 than in 2006 with the deepest point at levels 0.93 in 2004 and 0.83 in 2006. It also can be seen that the decrease of the emission intensity toward the higher velocities is somewhat slower in 2006 and similarly the depth of absorption is more pronounced for higher velocities in the 2006 low/hard state. The EW 0.54 Å of the absorption part of the P-Cyg profile in 2004 is canceled (with precision almost  $10^{-3}$  Å) by EW  $-0.54$  Å of the emission part of the profile. In 2006, the EW of P-Cyg absorption is +1.910 Å and emission  $-1.916$  Å. Note that these EWs refer to the disentangled mean seasonal profile, for which the noise is decreased and continuum is fitted to an extended spectral region. Consequently, their errors are smaller than those given in Table 1 for individual exposures (which are in the mean  $\pm 0.03$  Å and  $\pm 0.05$  Å in 2004 and 2006, respectively.). The continua of disentangled components may suffer from some complementary distortions induced by errors in rectification of the input spectra. The number of significant digits given here is to show that emission and absorption EWs of the P-Cyg component cancel each other out in both states within the precision of our data.

More remarkable difference is found between the disentangled profiles of the emission of the focused wind: its maximum is 0.056 in 2004, and 0.265 in 2006 in the units of the continuum level of the supergiant (a possible continuum of the focused wind cannot be disentangled, but it must be negligible compared with the continuum of the supergiant). Similarly, the mean EWs of the focused-wind emission are  $-0.33$  Å in 2004 and  $-1.78$  Å in 2006.

The line-strength factors, like the EWs, seem to show some phase-locked variations, which could reveal the geometry of the system (i.e., the distribution of the focused stellar wind in the space between the components) and eventually also the anisotropy of the deeper layers of the stellar wind in the upper atmosphere of the supergiant. However, the amplitude of these changes is comparable to the observational scatter and the phase coverage of our data is not yet sufficient, so we postpone this problem to our next study.



Our results generally confirm that it is the contribution of the focused wind, and not the P-Cyg profile formed in the root of the supergiant’s wind, that is responsible for the major part of the H $\alpha$  emission enhancement in the low/hard state compared with the high/soft state. The physics of this process will be discussed quantitatively in the following section.

## 4. DISCUSSIONS

### 4.1. The X-ray Excited Wind Model

The wind from isolated O and B stars is accelerated to a speed of approximately three times the escape velocity from the surface of the star by the force arising from the absorption and scattering of the photospheric continuum radiation in the ultraviolet resonance lines of abundant ions in the wind (Castor, Abbott & Klein 1975). The radiation driving force produces a velocity profile of

$$v(r) = v_\infty(1.0 - R_*/r)^\beta \quad (1)$$

in a steady state, where  $v(r)$  is the wind velocity at a distance of  $r$  from the center of the star,  $v_\infty$  is the terminal velocity of the stellar wind,  $R_*$  is the radius of the supergiant, and  $\beta \approx 0.8$  (Friend & Abbott 1986; Pauldrach et al. 1986). The gravitational effect of the compact companion in a massive X-ray binary system induces a stream of enhanced wind (focused stellar wind) in the line from the supergiant to the compact object. The level of the density enhancement in the focused wind is less than a factor of 2 as derived by Haberl et al. (1989), while Blondin et al. (1991) thought that the density in the focused wind was 20-30 times the ambient wind density. The presence of the focused wind in the massive X-ray binary could greatly enhance the mass accretion rate of the compact object in the system. Meanwhile, the X-ray radiation from the compact object can strongly influence the dynamics of the wind via X-ray heating and photoionization (Blondin et al. 1990, 1991).

The acceleration of the wind can be inhibited by the X-ray photoionization which can enhance the degree of ionization in the stellar wind. Thus, the deceleration of the wind due to the photoionization will greatly enhance the mass accretion of the compact object, which is a sensitive function of the wind velocity law,  $\dot{M}_{acc} \propto v^{-4}$ , and lead back to a higher X-ray luminosity. The temperature and ionization state of the stellar wind depend only on the “ionization parameter” (Kallman & McCray 1982),

$$\xi = L_x/n_p r_x^2, \quad (2)$$

where  $L_x$  is the X-ray luminosity of the compact object,  $n_p$  is the proton number density of the wind, and  $r_x$  is the distance to the X-ray source. When  $\xi \geq 10^2$  ergs cm s $^{-1}$ , the stellar wind will be strongly affected by X-ray ionization and when  $\xi \geq 10^3$  ergs cm s $^{-1}$ , X-ray heating will affect the dynamics of the wind (Blondin et al. 1990). To estimate the ionization parameter, let us suppose the wind of the supergiant to be spherically symmetric with a constant mass-loss rate,  $\dot{M} = 4\pi r^2 \mu m_p n_p(r) v(r)$ , where  $\mu$  is the mean atomic weight and  $m_p$  is the mass of the proton. Then

the ionization parameter in terms of the position and the stellar wind parameter can be derived (Sako et al. 1999),

$$\xi(r, r_x) = 4.3 \times 10^2 \frac{(L_x)_{36} (v_\infty)_8}{\dot{M}_{-7}} \left(\frac{r}{r_x}\right)^2 \left(1 - \frac{R_*}{r}\right)^\beta, \quad (3)$$

where  $(L_x)_{36}$  is the X-ray luminosity in a unit of  $10^{36}$  ergs  $s^{-1}$ ,  $(v_\infty)_8$  is the terminal velocity in a unit of  $10^8$  cm  $s^{-1}$ , and  $\dot{M}_{-7}$  is the mass loss of the supergiant in a unit of  $10^{-7} M_\odot \text{ yr}^{-1}$ .

Using the transformation formulae of Zdziarski et al. (2002), we can convert the RXTE/ASM one-day averaged counts in three bands (1.5-3, 3-5, and 5-12 keV) to the energy units. Adopting a distance of 2.5 kpc (Ninkov et al. 1987) to the source, we can get the X-ray luminosity of Cyg X-1 in different X-ray states. The mass-loss rate of the O9.7 supergiant is calculated by the formulae given by Howarth & Prinja (1989),  $\dot{M} = 2.0 \times 10^{-6} M_\odot \text{ yr}^{-1}$ . All parameters of Cyg X-1 are listed in Table 2. The ionization parameters during our 2001, 2003, 2004 and 2006 observational runs are calculated according to Equation (3) for two distances  $r_x = 21R_\odot$  and  $23R_\odot$  from the black hole and they are listed in Table 3. We also plot the contours of constant  $\xi$  ( $\xi = 10^2$ ) for Cyg X-1 in different X-ray states in Figure 6, where the coordinate origin is in the center of the supergiant, the thick circle is the surface of the supergiant, and the intersection of the two black dashed lines is the boundary of the supergiant’s Roche lobe.

#### 4.2. The Mass Accretion Rate in Different X-Ray States

The X-ray activity of the compact object is closely related to the mass accretion rate onto it. Since the supergiant component of Cyg X-1 has a negligible change in the  $H\alpha$  line between the low/hard and high/soft X-ray states, as discussed in the previous section, the mass-loss rate from the supergiant does not have an obvious change between these two types of X-ray states. One possible factor causing the enhancement of the mass accretion rate during the high/soft state may be the X-rays from the compact object. Figure 6 indicates that the ionization parameter  $\xi$  has a value of about  $100 \text{ ergs cm s}^{-1}$  at the position of  $r_x = 21R_\odot$  (in the line from the compact object to the supergiant) during the high/soft state, while it only has a value of  $11 \text{ ergs cm s}^{-1}$  during the low/hard state. Consequently, the focused wind may be photoionized by the X-ray during the high/soft state, which leads to the decrease of the radiative pressure exerted in lines by the supergiant’s own radiation, and hence also the velocity of the gas will be decreased. The slower wind velocity will greatly enhance the mass accretion of the compact object and a high X-ray luminosity will be observed during the high/soft state. During the low/hard state, the X-ray radiation is not strong enough to affect the focused wind, hence Cyg X-1 has a relatively low-mass accretion rate.

A related question we should discuss is which kind of mechanism causes Cyg X-1 to transit from the low/hard state to the high/soft state. Done (2002) suggested that the disk instability mechanism (DIM; Lasota (2001)) triggered the X-ray outburst and then the X-ray irradiation photoionized the hydrogen in the wind of the primary and enhanced the mass accretion onto the

compact object. The occurrence of the X-ray outburst does not have any periodicity and it may happen at any instant in the course of time. The duration of the outburst may be connected with the interaction between the X-rays from the compact object and the wind of the supergiant. In general, it can keep several weeks or even several months (see Figure 2).

### 4.3. The X-Ray Irradiation Effects on the H $\alpha$ Emission

X-ray heating could affect the dynamics of the wind from the supergiant. According to the plane-parallel model by Wu et al. (2001), a temperature-inversion layer will be formed in the stellar wind under the X-ray illumination. The temperature profile of the temperature-inversion layer is determined by the soft and hard X-ray irradiation. A strong temperature-inversion layer can be formed provided that the incident X-rays are soft and their angle of incidence is approaching grazing incidence. The more penetrating hard X-rays tend to heat up the deeper layers of the stellar wind.

During the high/soft state, the increased soft X-ray heating will increase the temperature of the ambient wind gas and then decrease the H $\alpha$  emissivity, which is proportional to  $T^{-1.2}$  (Richards & Ratliff 1998). The X-ray heating is more effective in the position near the X-ray source so the focused wind component in the Cyg X-1 is more easily affected by the X-ray radiation from the compact object. Thus, the focused-wind component in the H $\alpha$  line becomes weak during the X-ray high/soft state. During the low/hard state, the temperature profile of the focused wind is undisturbed by the X-ray irradiation and thus it has a strong emission in the H $\alpha$  line. Compared with the focused wind, the supergiant is farther from the X-ray source and its spherical wind is rarely influenced by the X-ray heating. However, when the X-ray luminosity is very high, the wind near the supergiant also can be affected (see Figure 6). For the high/soft state during our 2004 observational run the outer parts of the supergiant stellar wind were more ionized and thus unable to absorb and re-emit in H $\alpha$ . The terminal velocity of the wind also was smaller. For the low/hard state during our 2006 observational run, the soft X-rays from the compact object have almost no influence on the supergiant stellar wind. This could explain the small differences between the shapes of disentangled profiles in the two states in Figure 5. When the soft X-ray flux was very strong, the wind near the supergiant could also be influenced by the X-ray photoionization. Thus the system might lose its emission feature both in the supergiant and the focused-wind components. This scenario is consistent with the weak emission H $\alpha$  line in our 2001 spectra (on the bottom of Figure 1(a)).

During our 2004 observation, Cyg X-1 was also in a high/soft state, but the X-ray intensity was not so strong as that in our 2001 observations. Therefore, the focused-wind component in the H $\alpha$  line was at a lower emission level, while the supergiant component had a small change relative to the case in the low/hard state. Then we could observe an obvious P-Cygni H $\alpha$  profile during our 2004 observations. The spectra of Gies et al. (2003) and Tarasov et al. (2003) also indicate that the P-Cygni H $\alpha$  profile often appeared in the X-ray high/soft state. During the low/hard state, we rarely observed the P-Cygni structure in the complex H $\alpha$  line of Cyg X-1, because the focused-wind

H $\alpha$  component is strong enough to fill the absorption part of the P-Cygni line formed in the wind of the supergiant.

#### 4.4. The X-ray Flare During Our 2006 Observations

The H $\alpha$  EWs in our 2006 observational run are stronger than those in other runs (see Figure 2). Figure 1(d) shows that the focused-wind component in our 2006 H $\alpha$  spectra becomes very strong while the supergiant component is still in its normal emission level. Since the supergiant component did not have a significant change during our 2006 observations, it is inappropriate to explain the enhanced emission in the focused-wind H $\alpha$  component using the increased mass-loss rate from the supergiant. Figure 2 indicates that there is a small X-ray flare around the 2006 observational run. This X-ray flare was also detected by Swift/BAT in the 15-20 keV high-energy band. This phenomenon has been reported by Albert et al. (2007). Figure 7 shows the H $\alpha$  EW evolution during our 2006 observations and the light curves of the flare detected by RXTE/ASM and Swift/BAT, respectively. The dashed lines correspond to the beginning and the ending times of our 2006 observations.

This flare differs from the X-ray outburst during the high/soft state. It has a relatively low X-ray flux and a hard X-ray spectrum. The TeV emission also was detected during the flare by Albert et al. (2007) and they suggested that the flare was caused by the interaction between the jet and the stellar wind. Our observations were carried out on the decline phase of this flare. The weak soft X-ray emission during the flare is insufficient to form a prominent temperature-inversion layer in the focused-wind of Cyg X-1 and therefore a strong focused wind H $\alpha$  component was observed. However, the hard X-ray component during the flare could heat up the deeper layer of the focused wind and an extra H $\alpha$  emission could be detected during our spectroscopic observations. This can explain the strongest H $\alpha$  emission during our 2006 observations.

Another similar strong H $\alpha$  line with an EW of  $-2.315 \text{ \AA}$  was also observed by Tarasov et al. (2003) on MJD 5,0941.5449, when a small X-ray flare (low/hard state) was also detected by RXTE/ASM in the 1.5-12 keV band (see the inset in the top panel of Figure 7).

## 5. CONCLUSIONS

We present and analyze our optical spectroscopic observations of Cyg X-1 from 2001 to 2006. Combined with the RXTE/ASM X-ray observations, we make the following findings about this classical galactic black hole X-ray binary:

1. We confirm that the H $\alpha$  line shows two components: a P-Cygni profile moving with the radial velocity curve of the supergiant and a focused stellar wind component that moves with an approximately anti-phase orbital motion relative to the supergiant. The superposition of the

two components forms the complex  $H\alpha$  profiles.

2. The results of KOREL disentangling the  $H\alpha$  spectra during our 2004 and 2006 observations indicate that the focused-stellar wind is responsible for the major part of the  $H\alpha$  variability between different X-ray states. The focused wind component becomes strong during the X-ray low/hard state and weak during the high/soft state. The photoionization and heating of the X-ray photons from the compact object may affect the ionization state and dynamics of the wind from the supergiant. During the high/soft state, the X-ray photoionization could decelerate the gas in the focused stellar wind and result in an increasing mass accretion rate. During the low/hard state, the X-ray is not strong enough to influence the wind ionization state and the compact object has a low-mass accretion rate. The X-ray illumination can form a temperature-inversion layer in the stellar wind. During the high/soft state, the soft X-rays acting onto the focused stellar wind could increase its temperature greatly and thus decrease the  $H\alpha$  emissivity. This could explain the variability of the focused-wind component in  $H\alpha$  during different X-ray states. The strong soft X-ray emission during the high/soft state could also ionize the outer parts of the supergiant winds and render it unable to absorb and re-emit in  $H\alpha$ . This scenario is consistent with the small differences between the shapes of disentangled P-Cygni components in the 2004 and 2006 spectra. During our 2001 observations, the wind near the supergiant was also affected by the strong X-ray emission and an extremely weak  $H\alpha$  line was observed.
3. The  $H\alpha$  lines in our 2006 observations are very strong. We interpret this as the result of the low irradiation of the focused wind by the X-ray photons. The weak incident soft X-rays during the flare could not disturb the temperature profile of the focused stellar wind, while the hard X-rays could heat up the deep layer of the wind and an extra  $H\alpha$  emission could be observed.

J.Z.Y. is grateful to Min Fang for his help in plotting Figure 3 and Figure 6. This research is partially supported by the National Natural Science Foundation of China under grants 10433030 and 10673032. The work of PH has been done in the framework of the Center for Theoretical Astrophysics (ref. LC06014) with a support of grant GAČR 202/06/0041. The authors appreciate valuable comments by the referee.

## REFERENCES

- Albert, J., Aliu, E., Anderhub, H. et al. 2007, *ApJ*, 665 L51
- Bagnuolo, W. R., Jr., & Gies, D. R. 1991, *ApJ*, 376, 266
- Belloni, T., Méndez, M., van der Klis, M. et al. 1996, *ApJ*, 472, L107

- Blondin, J. M., Kallman, T. R., Fryxell, B. A., Taam, R. E. 1990, *ApJ*, 356, 591
- Blondin, J. M., Stevens, I. R., Kallman, T. R. 1991, *ApJ*, 371, 684
- Bolton, C. T. 1972, *Nature*, 235, 271
- Bowyer, S., Byram, E. T., Chubb, T. A., Friedman, H. 1965, *Sci*, 147, 394
- Brocksopp, C., Fender, R. P., Larionov, V. et al. 1999a, *MNRAS*, 309, 1063
- Brocksopp, C., Tarasov, A. E., Lyuty, V. M., & Roche, P. 1999b, *A&A*, 343, 861
- Castor, J. I., Abbott, D. C., Klein, R. I. 1975, *ApJ*, 195, 157
- Done, C. 2002, *Phil. Trans. R. Soc. A*, 360, 1967
- Friend, D. B. & Abbott, D. C. 1986, *ApJ*, 311, 701
- Friend, D. B. & Castor, J. I. 1982, *ApJ*, 261, 293
- Gallo, E., Fender, R., Kaiser, C. et al. 2005, *Nature*, 436, 819
- Gies, D. R. & Bolton, C. T. 1982, *ApJ*, 260, 240
- Gies, D. R. & Bolton, C. T. 1986a, *ApJ*, 304, 371
- Gies, D. R. & Bolton, C. T. 1986b, *ApJ*, 304, 389
- Gies, D. R., Bolton, C. T., Thomson, J. R. et al. 2003, *ApJ*, 583, 424
- Gies, D. R., Bolton, C. T., Blake, R. M. et al. 2008, *ApJ*, 678, 1237
- Haberl, F., White, N. E., Kallman, T. R. 1989, *ApJ*, 343, 409
- Hadrava, P. 1995, *A&AS*, 114, 393
- Hadrava, P. 1997, *A&AS*, 122, 581
- Hadrava, P. 2004, *Publ. Astron. Inst. ASCR*, 92, 15
- Hadrava, P. 2006, *A&AS*, 448, 1149
- Hadrava, P. 2007, in *Proceedings of RAGtime 8/9: Workshops on black holes and neutron stars*, ed. S. Hledík & Z. Stuchlík (Opava, Czech Republic: Silesian Univ.), 73 (arXiv:0710.0758)
- Herrero, A., Kudritzki, R. P., Gabler, R. et al. 1995, *A&A*, 297, 556
- Howarth, I. D. & Prinja, R. K. 1989, *ApJS*, 69, 527
- Iorio, L. 2007, arXiv:0707.3525

- Kallman, T. R. & McCray, R. 1982, *ApJS*, 50, 263
- Kemp, J. C., Barbour, M. S., Henson, G. D. et al. 1983, *ApJ*, 271, 65L
- Lachowicz, P., Zdziarski, A. A., Schwarzenberg-Czerny, A. et al. 2006, *MNRAS*, 368, 1025L
- LaSala, J., Charles, P. A., Smith, R. A. D., Bauciska-Church, M., & Church, M. J. 1998, *MNRAS*, 301, 285
- Lasota, J. P. 2001, *New Astro. Rev.*, 45, 449
- Malzac, J., Petrucci, P. O., Jourdain, E. et al. 2006, *A&A*, 448, 1125
- McClintock, J. E. & Remillard, R. A. 2006, in *Compact Stellar X-ray Sources*, ed. W. H. G. Lewin, M. van der Klis (Cambridge: Cambridge Univ. Press), 157 (astro-ph/0306213)
- Miller, J. M., Wojdowski, P., Schulz, N. S. et al. 2005, *ApJ*, 620, 398
- Mirabel, I. F. & Rodríguez, L. F. 1999, *ARA&A*, 37, 409
- Ninkov, Z., Walker, G. A. H. & Yang, S. 1987, *ApJ*, 321, 438
- Pauldrach, A., Puls, J., Kudritzki, R. P. 1986, *A&A*, 164, 86
- Pooley, G. 2001, *IAUC*, 7729, 3
- Priedhorsky, W. C., Terrell, J. & Holt, S. S. 1983, *ApJ*, 270, 233
- Puls, J., Kudritzki, R.-P., Herrero, A. et al. 1996, *A&A*, 305, 171
- Remillard, R. A. & McClintock, J. E. 2006, *ARA&A*, 44, 49
- Richards, M. T. & Ratliff, M. A. 1998, *ApJ*, 565, 447
- Russell, D. M., Fender, R. P., Gallo, E. & Kaiser, C.R. 2007, *MNRAS*, 376, 1341
- Sako, M., Liedahl, D. A., Kahn, S. M. & Paerels, F. 1999, *ApJ*, 525, 921
- Shaposhnikov, N. & Titarchuk, L. 2007 *ApJ*, 663, 445
- Sowers, J. W., Gies, D. R., Bagnuolo, W. G. et al. 1998, *ApJ*, 506, 424
- Stirling, A. M., Spencer, R. E., de la Force, C.J. et al. 2001, *MNRAS*, 327, 1273
- Tanaka Y. & Lewin W.H.G. 1995, in *X-ray Binaries*, ed. W. H. G. Lewin, J. van Paradijs, E. P. J. van den Heuvel (Cambridge: Cambridge Univ. Press), 126
- Tarasov, A. E., Brocksopp, C., Lyuty, V. M. 2003, *A&A*, 402, 237
- Walborn, N. R. 1973, *ApJ*, 179, L123

- Webster, B. L. & Murdin, P. 1972, *Nature*, 235, 37
- Wijers, R. A. M. J. & Pringle, J. E. 1999, *MNRAS*, 308, 207
- Wu, K., Soria, R., Hunstead, R. W., Johnston, H. M. 2001, *MNRAS*, 320, 177
- Yan, J. Z., Liu, Q. Z. & Hang, H. R. 2005, *ChJAA*, 5S, 247
- Zdziarski, A. A., Poutanen, J., Paciesas, W. S., Wen, L. Q. 2002, *ApJ*, 578, 357
- Zhang, S. N., Cui, W, Harmon, B. A. et al. 1997, *ApJ*, 477, L95
- Ziółkowski, J. 2005, *MNRAS*, 358, 851



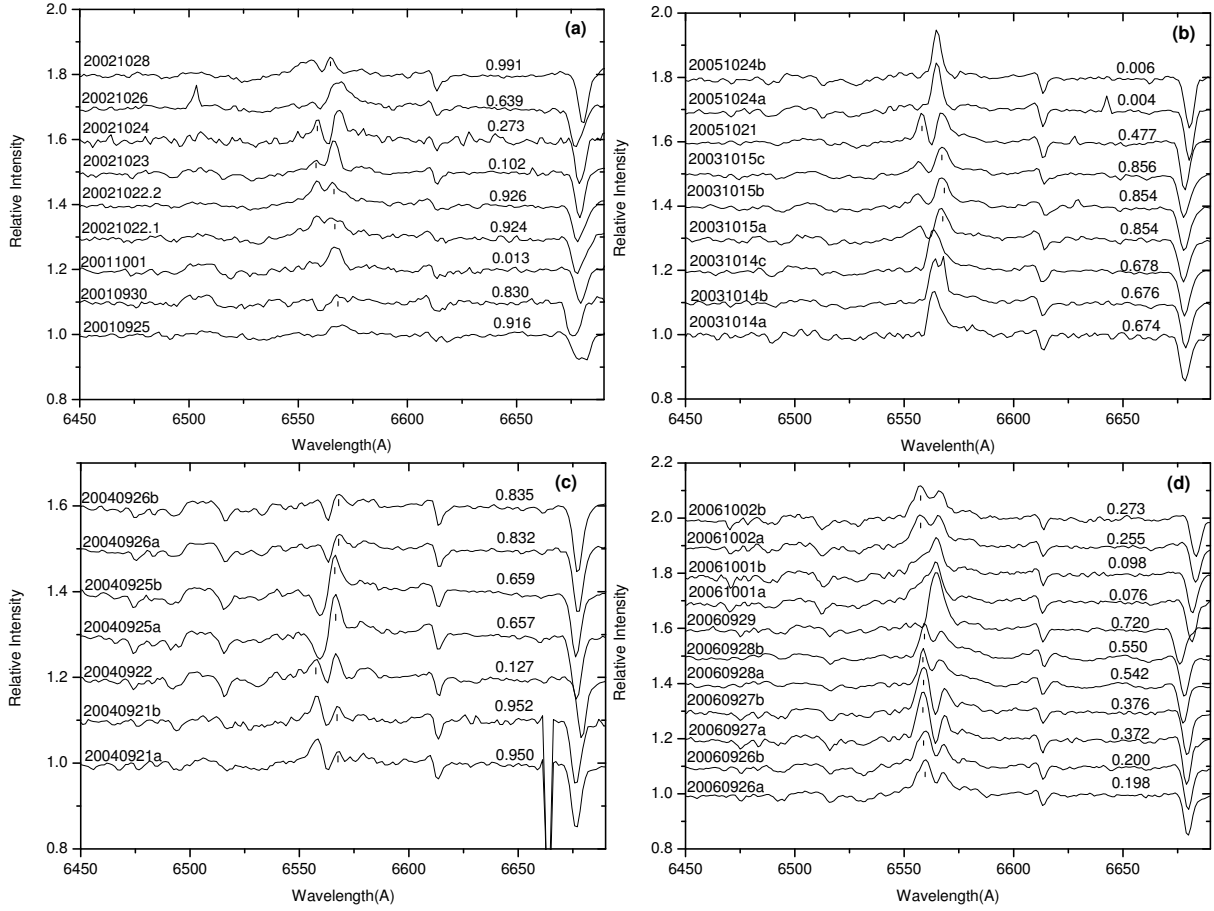


Fig. 1.— Spectra including H $\alpha$  and He I  $\lambda$ 6678 lines during six years’ observations. The observational dates and orbital phases are given in the left and right sides of each spectrum, respectively: (a) H $\alpha$  spectra in 2001 and 2002, (b) H $\alpha$  spectra in 2003 and 2005, (c) H $\alpha$  spectra in 2004, and (d) H $\alpha$  spectra in 2006. When the H $\alpha$  shows a double-peaked profile, the focused-wind component is marked by a tick in the figure.

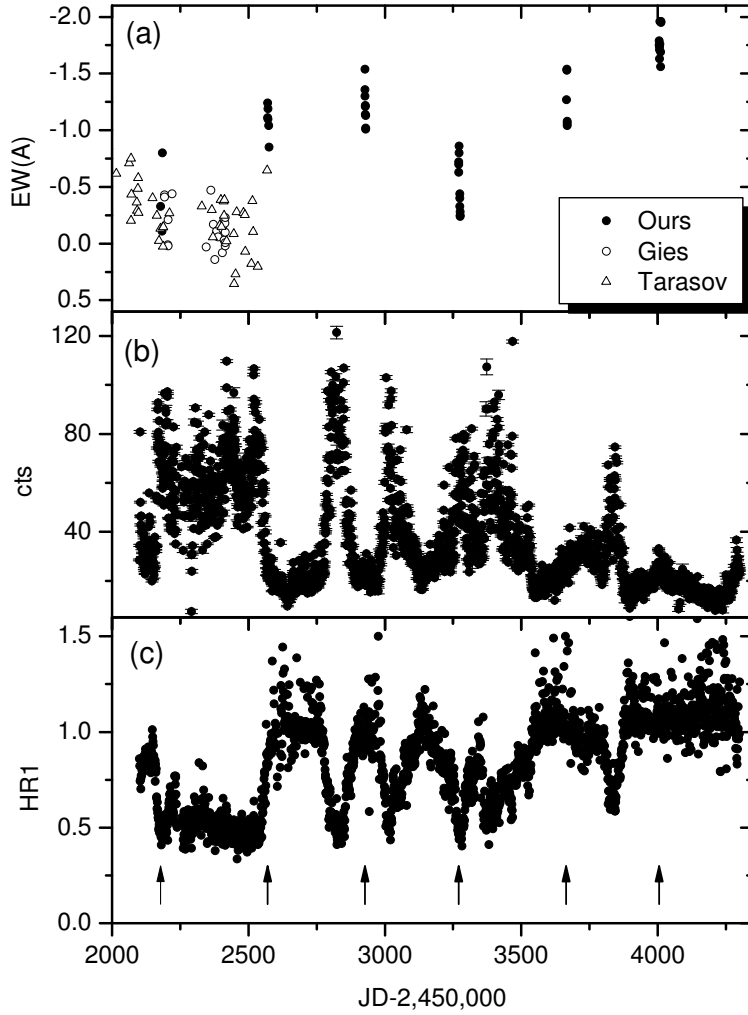


Fig. 2.— (a) H $\alpha$  EWs during six-year observations (filled circles). Data from Gies et al. (2003) (open circles) and Tarasov et al. (2003) (open triangles) are shown. (b) The one-day-averaged RXTE/ASM count rates of Cyg X-1 in 1.5-12 keV. (c) The hardness ratio in the soft X-ray band of RXTE/ASM, (3-5 keV)/(1.5-3 keV). The arrows on the bottom of the panel correspond to the starting time of each observational run.

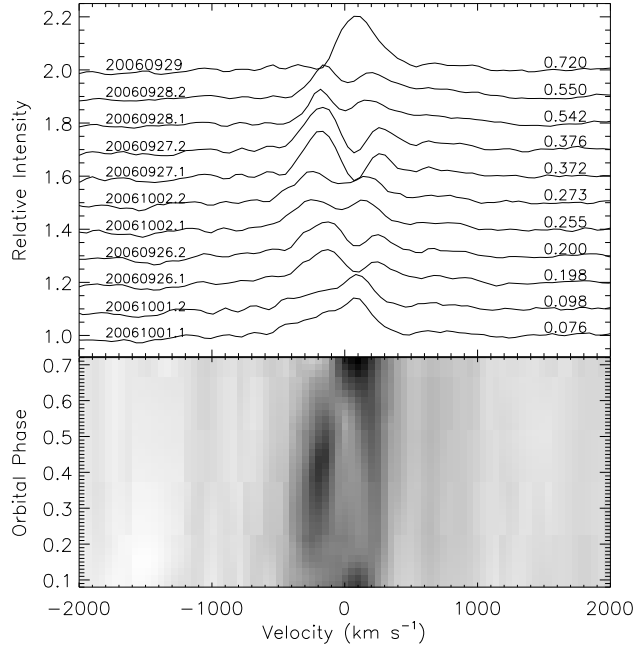


Fig. 3.— Top:  $H\alpha$  profiles during the 2006 observations, arranged in ascending order according to the orbital phase. The observational dates and orbital phases are given on each side of the  $H\alpha$ , respectively. All spectra have had the continuum level normalized and offset vertically to allow direct comparison. Bottom: the gray-scale map of the  $H\alpha$  spectra in 2006. The y-axis corresponds to the orbital phase and the gray intensity is scaled between 0.986 (white) and 1.17 (black).

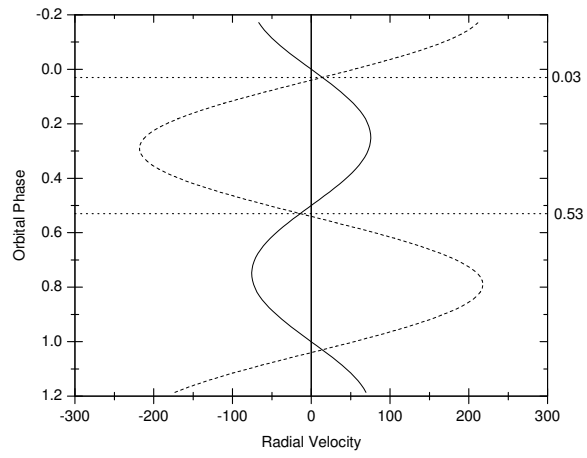


Fig. 4.— Radial velocity curves of the supergiant (solid line) and focused-wind (dotted line) components in the  $H\alpha$  line adopted from Gies et al. (2003). The two components have a comparative velocity around orbital phases  $\phi=0.03$  and  $0.53$ .

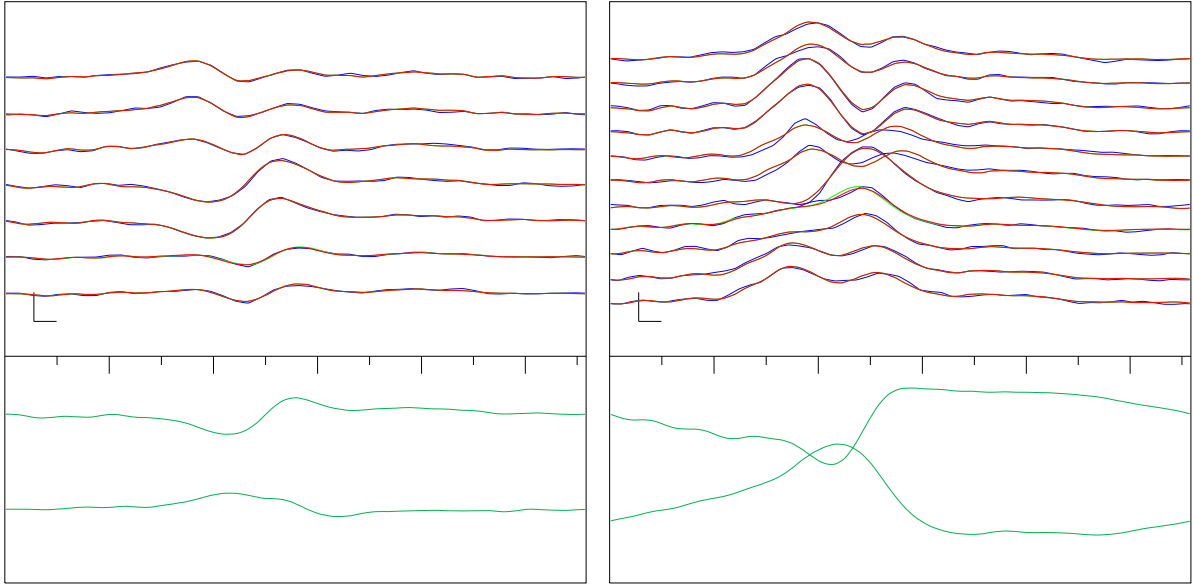


Fig. 5.— Disentangled  $H\alpha$  lines observed in high/soft state in the 2004 (left panel) and low/hard state in 2006 (right panel). The upper 7 lines (left panel) or 11 lines (right panel) indicate the input spectra ordered in running time from the top. These profiles are superimposed with their reconstruction as the sum of disentangled components, which are shown by the two bottom curves. The very bottom lines correspond to the emission of the focused stellar wind, which is obviously higher in 2006 than in 2004. The lines second from the bottom display the P-Cyg profiles of the supergiant. The maxima of their emission wings are practically equal in both states.

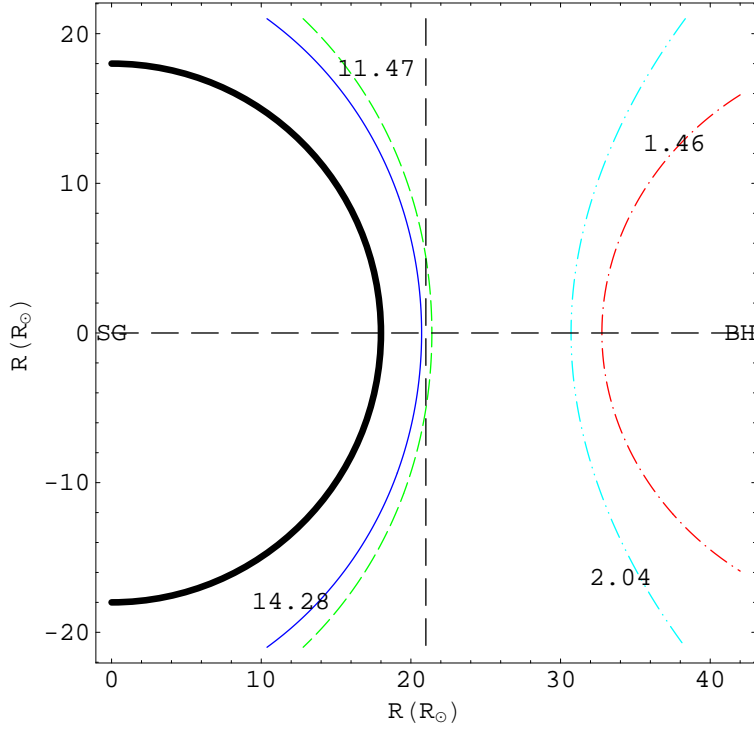


Fig. 6.— Contours of  $\xi=10^2$  for Cyg X-1 in different X-ray states. The coordinate origin is at the center of the supergiant and the thick circle represents the surface of the supergiant. The intersection of the two black dashed lines is the boundary of the supergiant’s Roche lobe. The solid, dashed, dot-dashed, and dot-dot-dashed lines are the contour lines when the X-ray luminosity  $(L_X)_{36}$  equals 14.28 (2001), 11.47 (2004), 1.46 (2003), and 2.04 (2006), respectively.

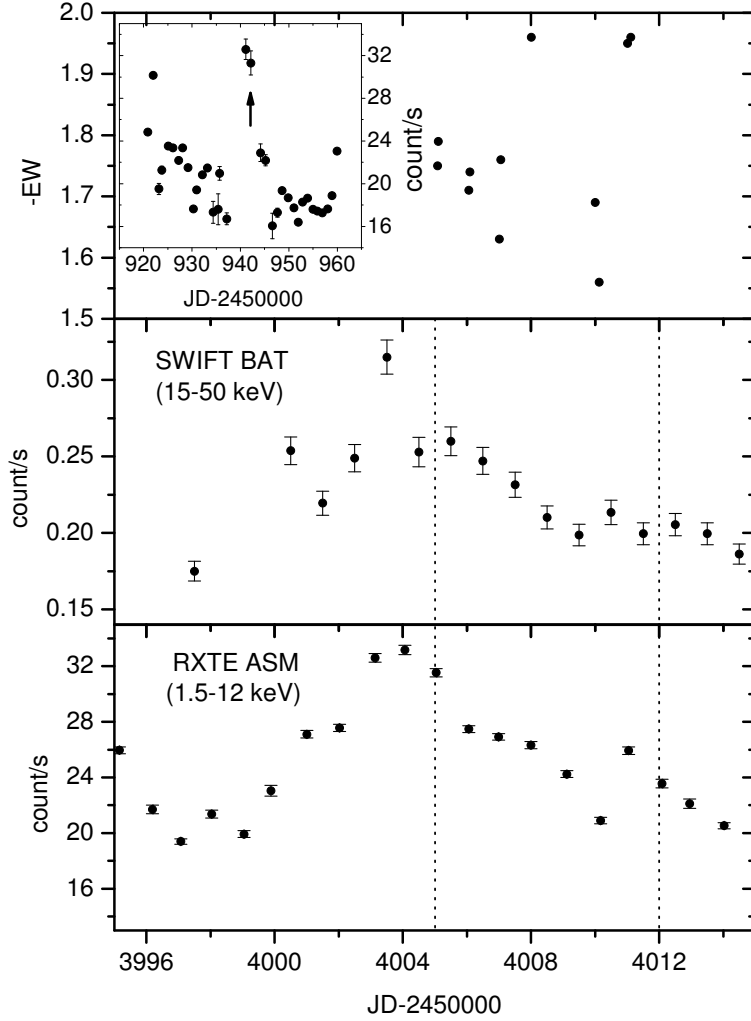


Fig. 7.— The top panel shows the  $H\alpha$  EWs during the 2006 observations. An X-ray flare was detected by Swift/BAT (15-50 keV) (middle) and RXTE/ASM (1.5-12 keV) (bottom) around our observations. The dashed lines correspond to the starting and ending times of the 2006 observations. The inset in the top panel is another X-ray flare detected by RXTE/ASM (1.5-12 keV) around MJD 50,941.5449 (the position of the arrow), when a strong  $H\alpha$  emission ( $-2.315 \text{ \AA}$ ) was observed by Tarasov et al. (2003).

Table 1. Summary of the spectroscopic observations of HDE 226868.

Date	UT Middle (hh:mm:ss)	Exposure Time (s)	Julian Date	Wavelength Range (Å)	Spectral Resolution Å pixel <sup>-1</sup>	Orbital Phase	H $\alpha$ EW (-Å)
20010925	11:10:26	300	2452177.9656	5550-6750	1.22	0.916	0.33±0.02
20010927	12:06:13	400	2452180.0043	4300-5500	1.22	0.280	–
20010930	13:59:44	300	2452183.0832	5550-6750	1.22	0.830	0.11±0.01
20011001	14:35:41	300	2452184.1081	5550-6750	1.22	0.013	0.80±0.02
20021022	12:01:07	300	2452570.0008	5550-6750	1.22	0.925	1.11±0.14
20021022	12:11:09	800	2452570.0077	5550-6750	1.22	0.926	1.24±0.09
20021023	11:53:21	500	2452570.9954	5550-6750	1.22	0.102	1.10±0.11
20021024	10:50:35	600	2452571.9518	5550-6750	1.22	0.273	1.19±0.08
20021026	12:01:53	500	2452574.0013	5550-6750	1.22	0.639	1.04±0.05
20021027	11:39:28	500	2452574.9857	4300-5500	1.22	0.815	–
20021028	11:23:20	500	2452575.9745	5550-6750	1.22	0.991	0.85±0.11
20031014	11:44:08	300	2452926.9890	5550-6750	1.22	0.674	1.36±0.04
20031014	11:53:48	800	2452926.9957	5550-6750	1.22	0.676	1.54±0.04
20031014	12:09:23	1000	2452927.0065	5550-6750	1.22	0.678	1.30±0.04
20031015	11:48:38	300	2452927.9921	5550-6750	1.22	0.854	1.22±0.03
20031015	11:56:49	500	2452927.9978	5550-6750	1.22	0.855	1.21±0.07
20031015	12:05:49	500	2452928.0040	5550-6750	1.22	0.856	1.14±0.04
20031016	11:44:54	20	2452928.9895	4300-6700	2.44	0.032	1.13±0.06
20031016	11:46:34	100	2452928.9907	4300-6700	2.44	0.032	1.01±0.02
20031016	11:48:20	50	2452928.9919	4300-6700	2.44	0.032	1.02±0.02
20040921	14:53:34	900	2453270.1205	5550-6750	1.22	0.950	0.72±0.08
20040921	15:09:20	900	2453270.1315	5550-6750	1.22	0.952	0.63±0.06
20040922	14:43:41	900	2453271.1137	5550-6750	1.22	0.127	0.80±0.04
20040923	11:35:11	600	2453271.9828	4300-6700	1.22	0.282	0.86±0.01
20040925	13:55:31	1000	2453274.0802	5550-6750	1.22	0.657	0.44±0.01
20040925	14:13:04	1000	2453274.0924	5550-6750	1.22	0.659	0.40±0.03
20040926	13:31:28	1000	2453275.0635	5550-6750	1.22	0.832	0.28±0.01
20040926	13:49:02	1000	2453275.0757	5550-6750	1.22	0.835	0.25±0.01
20051021	13:30:33	900	2453665.0629	5550-6750	1.22	0.477	1.27±0.04
20051023	11:31:50	100	2453666.9804	4300-6700	2.44	0.820	1.53±0.06
20051023	11:34:05	100	2453666.9820	4300-6700	2.44	0.820	1.54±0.01



Table 1—Continued

Date	UT Middle (hh:mm:ss)	Exposure Time (s)	Julian Date	Wavelength Range (Å)	Spectral Resolution Å pixel <sup>-1</sup>	Orbital Phase	H $\alpha$ EW (-Å)
20051024	12:17:10	900	2453668.0119	5550-6750	1.22	0.004	1.04±0.02
20051024	12:32:50	900	2453668.0228	5550-6750	1.22	0.006	1.08±0.02
20051027	12:56:50	600	2453671.0395	4300-5500	1.22	0.545	–
20060926	14:05:43	1200	2454005.0873	5550-6750	1.02	0.198	1.75±0.07
20060926	14:27:18	1200	2454005.1023	5550-6750	1.02	0.200	1.79±0.06
20060927	13:26:20	1200	2454006.0600	5550-6750	1.02	0.372	1.71±0.02
20060927	14:05:07	1200	2454006.0869	5550-6750	1.02	0.376	1.74±0.07
20060928	12:24:02	1200	2454007.0167	5550-6750	1.02	0.542	1.63±0.09
20060928	13:25:46	1200	2454007.0596	5550-6750	1.02	0.550	1.76±0.08
20060929	12:19:54	1200	2454008.0138	5550-6750	1.02	0.720	1.96±0.03
20060930	13:28:44	1200	2454009.0616	3850-5050	1.02	0.908	–
20061001	12:04:59	600	2454010.0035	5550-6750	1.02	0.076	1.69±0.02
20061001	15:09:09	600	2454010.1314	5550-6750	1.02	0.099	1.56±0.03
20061002	12:09:59	600	2454011.0069	5550-6750	1.02	0.255	1.95±0.04
20061002	14:35:00	600	2454011.1076	5550-6750	1.02	0.273	1.96±0.03

*Note* The ephemeris is adopted from Gies et al. (2003).

Table 2: Parameters of Cyg X-1

Parameter	Value	Reference
$M_*$	24±5 $M_\odot$	Iorio (2007)
$M_x$	8.7±0.8 $M_\odot$	Shaposhnikov & Titarchuk (2007)
q= $M_x/M_*$	0.36±0.05	Gies et al. (2003)
$a$	42±9 $R_\odot$	Iorio (2007)
$i$	48.0±6.8°	Iorio (2007)
Roche lobe size	$r_m=21±6 R_\odot$	Iorio (2007)
$V_\infty$	1700 km s <sup>-1</sup>	-
$T_*$	40,000K	-
$d$	2.5 kpc	Ninkov et al. (1987)
$L_{opt}/L_\odot$	5.59×10 <sup>5</sup>	Ziółkowski (2005)
$\dot{M}_w$	2.0×10 <sup>-6</sup> $M_\odot$ yr <sup>-1</sup>	Howarth & Prinja (1989)
$R_*$	18 $R_\odot$	-

Table 3: Ionization parameters in different X-ray states

Observational Run	X-ray State	X-ray luminosity ( $10^{36}$ ergs $s^{-1}$ )	$\xi(r_x=21R_\odot)$ (ergs cm $s^{-1}$ )	$\xi(r_x=23R_\odot)$ (ergs cm $s^{-1}$ )
2001	High/Soft	14.28	110.04	40.89
2003	Low/Hard	1.46	11.25	4.18
2004	High/Soft	11.47	88.38	32.84
2006	Low/Hard	2.04	15.72	5.84